DOI: 10.13009/EUCASS2023-506
Aerospace Europe Conference 2023 – 10TH EUCASS – 9TH CEAS

Sensitivity Study on a Low Order Model for the Analysis of Transverse Combustion Instability

Alessandro Montanari[⋆†], *Paolo Maria Zolla*[⋆], *Simone D'Alessandro*[⋆⋆], *Marco Pizzarelli*[⋆⋆], *Francesco Nasuti*[⋆], *Rocco Carmine Pellegrini*[⋆⋆] *and Enrico Cavallini* [⋆⋆]
[⋆]*Sapienza University of Rome*
Via Eudossiana 18, 00184, Rome, Italy
alessandro.montanari@uniroma1.it, paolomaria.zolla@uniroma1.it, francesco.nasuti@uniroma1.it
[⋆⋆]*The Italian Space Agency (ASI)*
Via del Politecnico snc, 00133, Rome, Italy
simone.dalessandro@asi.it, marco.pizzarelli@asi.it, rocco.pellegrini@asi.it, enrico.cavallini@asi.it
[†]Corresponding author

Abstract

The present paper investigates transverse combustion instability in multi-injector engines using a low-order modeling approach. It combines one-dimensional injector modeling, three-dimensional combustion chamber modeling, and a response function that mimics the fuel accumulation mechanism sustaining instability in liquid rocket engines with coaxial injectors. The analysis focuses primarily on the impact of the response function parameters on the resulting limit cycle frequency and amplitude. Experimental data from an 82-injector LOX/Methane engine afflicted by transverse instability are used to this goal. The study also explores the possible damping of thermoacoustic phenomena through the use of baffles. Results yield valuable insights into the response function behavior in geometrically complex scenarios and highlight the effectiveness of low-order models as design tools for liquid rocket engines.

1. Introduction

In the context of liquid rocket engines (LREs), combustion or thermoacoustic instability (CI) is one of the most insidious phenomena to be faced during the design phase. Resulting from a complex feedback coupling of acoustics, hydrodynamics and heat release, it manifests as self-sustained pressure oscillations with a defined spectrum and a peak-to-peak amplitude greater than 10% of the mean chamber pressure [1]. Following a classification based on the frequency of fluctuations, the most harmful instability is the high-frequency (HF) one (> 1 kHz), also called "screaming", characterized by the interaction between unsteady combustion and chamber acoustic modes. These intense acoustic oscillations give rise to unexpected mechanical and thermal loads, which can lead to catastrophic system failure. Despite several years of research since the late '50s [2], the complex multi-physics mechanism that drives the instability is not yet fully understood. Hence, there is a strong need to enhance our understanding and develop reliable predictive tools in order to mitigate risks and minimize costs associated with the development of new engines.

Nowadays, HF combustion instability is studied through a synergic approach combining lab-scale experiments and a hierarchy of numerical models. As far as experiments are concerned, years of testing have demonstrated that the stability of a LRE is largely affected by the injector design [1]. In particular, shear coaxial injectors, commonly used in liquid oxygen/hydrogen (LOX/H_2) and liquid oxygen/methane (LOX/CH_4) systems, have been extensively addressed. Within this context, the acoustics of the oxidizer flow has shown to be a key element for thermoacoustic coupling, with several experimental campaigns evidencing a strict relationship between the heat release rate spectrum and the oxidizer-post longitudinal acoustic spectrum, suggesting a modulation of unsteady combustion by axial pressure waves in the injectors [3, 4, 5].

In parallel with experiments, screaming is investigated through high-fidelity numerical simulations, namely Large Eddy Simulations (LESs) and Detached Eddy Simulations (DESs) [6, 7, 8], which offer the possibility to get valuable insights into the phenomenon. More specifically, DESs simulations have shown that the instability in coaxial injectors can be driven by fuel accumulation and release [7]. Such fuel dynamics can be primarily attributed to the intrinsic characteristics of these injectors. Indeed, they work by design with a strong radial density gradient in the recess zone, i.e. the region where oxidizer and fuel mix with each other. The interaction of this radial density gradient with axial pressure gradients due to the propagation of acoustic disturbances into the injectors gives rise to baroclinic

DOI: 10.13009/EUCASS2023-506

Figure 1: Interaction between longitudinal pressure gradient and radial density gradient in a typical shear coaxial injector. Image credit: [7].

torque ($\nabla\rho \times \nabla p$), that acts as a vorticity source (Figure 1). If pressure waves are strong enough, they might cause vortexes to intensify and the flow to slow down. The resulting phenomenology is a cyclic disruption and release of fuel pockets from the recess, that locally modifies the mixture ratio (O/F) in the chamber, potentially closing the feedback loop by generation of new acoustic waves provided that the release frequency locks-in with a chamber eigenmode.

Although unique to reveal details of the combustion instability dynamics, both sub-scale experiments and high-fidelity computations can hardly be considered suitable for the design of new engines. The former are indeed not representative of full-scale LREs stability, since instability is highly sensitive to the engine size. On the other hand, the latter are not fully reliable, since they always include some modeling that can lead to a lack of predictivity [6], in addition to being extremely expensive in terms of computational time.

For these reasons, research has moved toward the so-called low-order models, in which low computational costs are achieved employing a simplified physics. However, such a reduction in complexity can negatively impact the detection of thermoacoustic coupling, which is therefore enforced by incorporating a response function (RF) into the governing equations. The ultimate goal of a low-order model is to achieve fast and quite accurate evaluation of chamber stability behavior by effectively capturing the primary driving phenomenology of thermoacoustic combustion instability. Thus, a crucial element of this modeling approach is the determination of the response function. The derivation of response functions typically relies on the analysis of experimental data or high-fidelity simulations. A widespread approach is the $n-\tau$ model, based on Crocco's time-lag theory [9], which establishes a direct link between acoustic and heat release fluctuations through a proportionality index n, assuming a time-lag τ. Several examples of this approach are available in literature, showing in general good capabilities in reproducing high-fidelity data and experiments, provided a suitable tuning of the aforementioned parameters [10, 11].

A more physically-aware RF is the one by D'Alessandro et al. [12], which mimics the fuel modulation mechanism in shear coaxial injectors by linking the injected fuel mass flow rate to pressure fluctuations in the recess, closing indirectly the feedback loop. Despite its simplicity, this approach has properly captured longitudinal and transverse instabilities in both ideal and real gas Eulerian frameworks [12, 13, 14], demonstrating the possible use of low-order models as design tools for LREs. This formulation includes several parameters, whose calibration has shown to be crucial to predict longitudinal instability in a quasi-1D modeling context [12]. However, a noteworthy aspect of this RF formulation is that said tuning does not rely on any high-fidelity or experimental data. It is therefore clear how such a low-order model has potential to be used as a standalone tool for LREs design.

The present work aims to extend the response function sensitivity analysis to a more complex scenario, specifically the one of transverse combustion instability in multi-injector engines, more representative of real engine conditions, with the objective of correctly reconstructing experimental data from unstable LREs. In order to study transverse combustion instability in a low-order fashion, the hybrid 1D-3D (or hybrid-D) approach presented in [15] is followed. Moreover, an important part of the paper deals with the modeling and implementation of baffles, which are one of the most common damping devices employed to "cure" transversally unstable engines [16].

The paper is organized as follows: Section § 2 describes in detail the governing equations (§ 2.1), the response function (§ 2.2), and the hybrid-D approach (§ 2.3) used in the low-order model. Section § 3 is dedicated to the presentation of the experimental test case afflicted by spontaneous transverse combustion instability selected as test bench for model analysis. In Section § 4, results are presented, with an overview of the phenomenological aspects captured by the present approach (§ 4.1), followed by a thorough sensitivity analysis of the RF main parameters (§ 4.2). Lastly, the implementation of baffles and the resulting instability prediction and characteristics are the subject of Section § 4.3.

2. Mathematical model

In principle, the study of transverse combustion instability would require a 3D description of the whole system. However, the flow dynamics taking place in rocket engine injectors is basically one-dimensional. Such aspect justifies an

DOI: 10.13009/EUCASS2023-506

approach based on the splitting of the computational domain into two sub-domains: chamber and injectors. While the chamber is handled by an existing, already validated in-house software for three-dimensional multi-species flows [17], each injector is modeled as a quasi-1D (Q1D, i.e. one-dimensional domain with variable cross-sectional area) domain. This paper describes in detail only the Q1D modeling, where the response function is embedded. Description of the 3D solver is omitted, since it is based on the well-known 3D ideal Eulerian model.

2.1 Governing equations

The governing equations are the quasi-1D multi-species Euler equations. Three chemical species are taken into account, i.e. fuel, oxidizer, and combustion products (subscript "ox" for oxidizer, "f" for fuel, and "p" for combustion products). Even if combustion instability is characterized by strong variations in mixture ratio, i.e. strong differences in terms of combustion products composition, said products are represented by a single species having the properties of the mixture of the main resulting species as computed by CEA software [18] at stoichiometric conditions. This modeling choice allows an important reduction in computational cost. The governing equations read as:

$$\begin{cases} (\rho A)_t + (\rho u A)_x = \dot{\omega}_{f1} & (1) \\ (\rho u A)_t + \left[\left(\rho u^2 + p\right) A\right]_x - p A_x = u \dot{\omega}_{f1} & (2) \\ (\rho A Y_{ox})_t + (\rho u A Y_{ox})_x = \dot{\omega}_{ox} & (3) \\ \left(\rho A Y_f\right)_t + \left(\rho u A Y_f\right)_x = \dot{\omega}_{f1} + \dot{\omega}_{f2} & (4) \\ (\rho e_0 A)_t + (\rho u h_0 A)_x = \dot{\omega}_{f1} h_{0f} + \left(\dot{\omega}_{ox} \Delta h^0_{f,ox} + \dot{\omega}_{f2} \Delta h^0_{f,f} - \dot{\omega}_p \Delta h^0_{f,p}\right) & (5) \end{cases}$$

where ρ, u, p, Y_{ox}, and Y_f are, respectively, density, velocity, pressure, and mass fractions of oxidizer and fuel, while e_0 and h_0 are the specific total internal energy and total enthalpy.

Several source terms characterize the right-hand side of Equations 1-5, representing the contribution of combustion and mass addition in the recess. Regarding the combustion source term in Equation 5, treated in the same way in both the quasi-1D and 3D domains, $\Delta h^0_{f,i}$ is the the standard formation enthalpy of the $i-th$ species, while $\dot{\omega}_i$ is the rate of production per unit length of the $i-th$ species. To properly take into account phenomena such as mixing, atomizazion, and vaporization, combustion is inhibited in the domain up to an abscissa x_c measured from the backstep. The combustion reaction is modeled as an Arrhenius-like first-order reaction between the fuel and the oxidizer:

$$\begin{cases} \dot{\omega}_{f2} = -\dfrac{\dot{m} Y_o Y_f}{\delta} e^{-T_r/T} & \text{if} \quad x > x_c \\ \dot{\omega}_{f2} = 0 & \text{otherwise} \end{cases} \tag{6}$$

where δ and T_r are tuning parameters through which the heat release curve can be modified, and $\dot{m}$ is the local mass flow rate. It is assumed that the oxidizer reacts with the fuel at a stoichiometric proportion:

$$\dot{\omega}_{ox} = (O/F)_{\text{st}}\, \dot{\omega}_{f2} \tag{7}$$

Concerning mass addition, fuel is introduced in the recess in a length l_f assuming a constant mass flow rate per unit length $\dot{\omega}_{f1}$:

$$\dot{\omega}_{f1} = \frac{\dot{m}_f}{l_f} \tag{8}$$

where $\dot{m}_f$ is the overall injected fuel mass flow rate. Oxidizer is instead introduced at the left boundary, where oxidizer mass flow rate and stagnation temperature are enforced as boundary conditions for the subsonic inlet.

Numerical integration of the described equations is performed by discretizing them through a finite volume method. The numerical fluxes are calculated employing the Glaister version of the Roe approximated Riemann solver [19]. Second-order accuracy in space and time is achieved through a Godunov-like integration approach, including MinMod reconstruction in both space and time.

DOI: 10.13009/EUCASS2023-506

2.2 Response function

As thoroughly explained in Section § 1, low-order models need a so-called response function to properly capture the thermoacoustic feedback loop. Following the approach described in [12], based on the mimicking of the fuel accumulation/release dynamics that characterize shear coaxial injectors, the fuel mass flow rate oscillations are linked to pressure oscillations as follows:

$$\dot{m}_f = \dot{m}_{f,0} + \dot{m}'_f \tag{9}$$

$$\dot{m}'_f = \min\left[\hat{\dot{m}}'_f, \frac{m_{f,acc}}{\delta t}\right] \qquad \text{where} \qquad \hat{\dot{m}}'_f = \dot{m}_{f,0}\left[\exp\left(-\sigma\,\frac{p(t,x_s) - p_0(t,x_s)}{p_0(t,x_s)}\right) - 1\right] \tag{10}$$

where $\dot{m}'_f$ is the fuel mass flow rate fluctuation induced by acoustic propagation in the injectors, σ is a proportionality factor, x_s is the abscissa where pressure is sampled (measured from the recess starting abscissa), p_0 is the mean pressure at the sampling point (x_s), and $m_{f,acc}$ is the instantaneous fuel mass trapped into the pocket at the recess, introduced to ensure mass conservation and computed at runtime as:

$$m_{f,acc} = \int_0^t -\dot{m}'_f \mathrm{d}t \tag{11}$$

2.3 Hybrid-D approach

A key characteristic of the present low-order model is the capability to describe multi-injector geometries treating each injector as a quasi-1D domain, while retaining the 3D nature of the combustion chamber in order to capture transverse gasdynamics phenomena. This modeling solution reduces significantly the computational burden but requires an accurate treatment of the connection between the sub-domains. Specifically, the interface between the quasi-1D and 3D regions is treated in the following manner (Figure 2): a certain surface $\mathcal{B}_j$ is connected to the $j-th$ injector. The numerical fluxes are computed between each cell of the 3D domain constituting the $\mathcal{B}_j$ surface and the rightmost cell of the $j-th$ quasi-1D domain, assuming null momentum fluxes in the y- and z- directions (i.e. axial flow in the injectors). Then, the mass, x-momentum, and energy fluxes are integrated over $\mathcal{B}_j$ in order to be added to the quasi-1D cell.

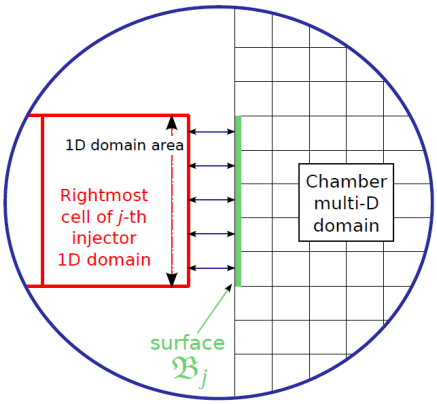

(a) Sub-domains interface.

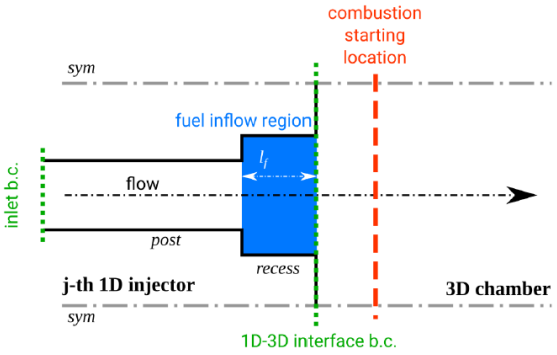

(b) Schematic of a hybrid-D domain.

Figure 2: Domain splitting.

3. The NASA-LeRC test case

The engine used as test bench in the present work was developed as part of the LOX/Hydrocarbon Combustion Instability Investigation Program at NASA in 1989 (NAS3-24612 [5]). The main goal of this experimental campaign was to assess the stability characteristics of the LOX/CH_4 propellant combination compared to LOX/H_2.

DOI: 10.13009/EUCASS2023-506

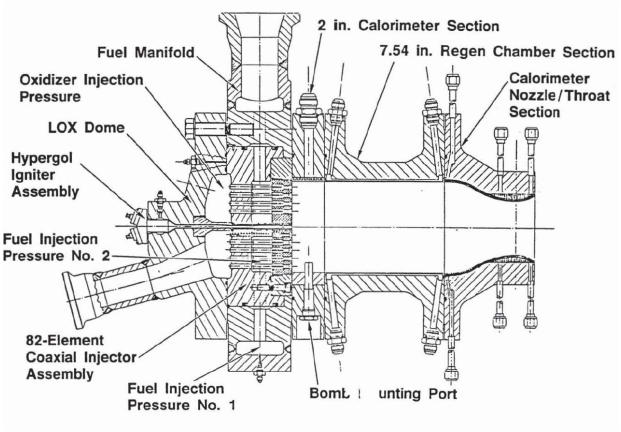

(a) Thrust chamber assembly.

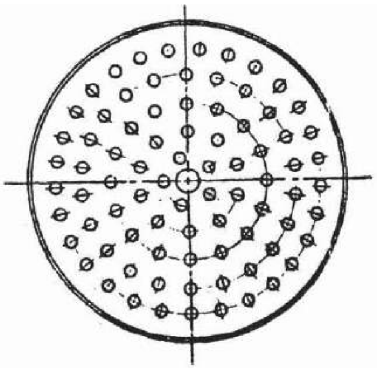

(b) Injection plate.

Figure 3: Geometrical details of the NASA-LeRC design [5].

Table 1: NASA-LeRC geometrical data

Parameter	Value
Number of injectors	82
Post inner diameter, mm	3.4
Post outer diameter, mm	4.6
Post length, mm	91.6
Recess diameter, mm	5.71
Recess length, mm	5.13
Chamber diameter, mm	143.8
Chamber length, mm	242.3
Throat diameter, mm	84
Contraction ratio	2.92
Nozzle length, mm	143.2

The thrust chamber employed in this program at NASA Lewis Research Center (nowadays Glenn Research Center) belongs to the class of 178 kN of thrust, often used in U.S. combustion instability studies [1]. The engine, referred in the following as NASA-LeRC, consists of a combustion chamber with a diameter of 14.38 cm, where propellants are injected through a system of 82 recessed shear coaxial injectors. The oxidizer post length is equal to 9.16 cm, while the recess measures 5.13 mm. The cylindrical part of the chamber has a length of 24.23 cm and is followed by a 14.32 cm long convergent-divergent nozzle, with a contraction ratio equal to 2.92. Details of the thrust chamber assembly and injection plate can be seen in Figure 3, while geometrical data are reported in Table 1.

A total of 17 tests have been performed in this campaign varying from case to case the engine load point. Specifically, the mixture ratio was varied in the range 2.5 - 3.7, hence employing in all cases a fuel-rich mixture, while the nominal chamber pressure was ~13.8 MPa. Out of these 17 tests, six of them investigated spontaneous instability onset and, among them, two resulted in unstable operations. In particular, the spectrum of the pressure signals recorded during these two experiments evidenced that the majority of the power spectral density was centered around the first tangential mode (1T) of the chamber (5.2 kHz). For the purpose of studying tangential instability phenomena, load point “Test 014-004” represents an ideal candidate and is therefore chosen as reference. The operational conditions of the selected load point are reported in Table 2.

4. Results

4.1 Numerical setup and reference results

An important peculiarity of the selected test case is that the oxygen in the post is at supercritical pressure and subcritical temperature, in a so-called dense fluid state. This condition results in a thermodynamic behavior that strongly deviates

DOI: 10.13009/EUCASS2023-506

Table 2: "Test 014-004" load point

Parameter	Value
Nominal chamber pressure, MPa	13.3
Mixture ratio	3.12
Oxidizer mass flow rate, kg/s	30.9
Fuel mass flow rate, kg/s	9.9
Oxidizer injection temperature, K	115.4
Fuel injection temperature, K	275.4
Instability frequency, Hz	5200 (1T)
Instability peak-to-peak amplitude, MPa	20.7 (150% p_c)

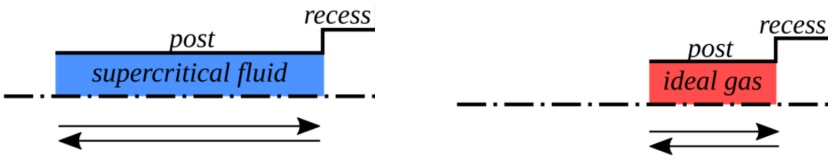

Figure 4: Acoustic rescaling of the oxidizer post.

from the one described by the ideal gas law, especially in terms of speed of sound [20], a key quantity in thermoacoustic dynamics. Therefore, a proper thermodynamic modeling through a real-fluid equation of state should be used [13]. However, the goal of the present paper is to analyze the behavior of the response function in a geometrically complex scenario, but avoiding the numerical burden introduced by a real-fluid treatment. To this aim, the supercritical propellant is replaced with thermally perfect gas, retaining the LOX injection temperature (115.4 K). In order to preserve the acoustic features of the injector within an ideal gas framework, the length of the oxidizer post needs to be rescaled such that the injector frequency in the ideal case matches the injector frequency in the real case:

$$\left(\frac{L_p}{u+a}+\frac{L_p}{a-u}\right)_{ideal}=\left(\frac{L_p}{u+a}+\frac{L_p}{a-u}\right)_{real} \tag{12}$$

where L_p is the post length, a is the speed of sound, and u the axial velocity. This "acoustically equivalent" version of the injector yields an oxidizer post length of 19.39 mm (Figure 4), as expected shorter with respect to the real one.

In the hybrid-D model, the injectors are represented by 82 nearly identical quasi-1D domains, each discretized with 500 equispaced cells. On the other hand, the combustion chamber is described by a three-dimensional domain, with approximately 400k cells. Details regarding the domain geometry and its discretization can be found in Figure 5. Particularly, Figure 5a illustrates the significant axial mesh refinement near the injection plate. This careful mesh arrangement is necessary to avoid resolution issues of convected fuel pockets in the region of the chamber before combustion ($x < x_c$). Indeed, this part of the 3D domain is characterized by low flow velocity ($\sim$ 10 m/s). This fact, together with the high frequencies characterizing thermoacoustic phenomena, translates into a small spatial wavelength of the convected fuel pockets. In order to properly resolve the convection of these high wavenumber entropy waves, a sufficient number of cells must be employed in the region of interest. Specifically, the axial cell size has been selected in order to capture each fuel pocket with 15 cells.

It is worth to remind that an appropriate choice of the model free parameters, as described in Section § 2, is crucial for its application. Initially, the number of parameters is reduced by eliminating the dependence on the pressure sampling abscissa (x_s). This modification in the formulation is obtained by redefining the sampled pressure value $p(x_s,t)$ and the reference pressure value $p_0(t)$, which are no longer sampled at a specific abscissa x_s, but rather averaged over the entire recess:

$$\hat{\dot{m}}'_f=\dot{m}_{f,0}\left[\exp\left(-\sigma\,\frac{\overline{p}(t)-\overline{p}_0(t)}{\overline{p}_0(t)}\right)-1\right] \qquad \text{where} \qquad \overline{f}(t)=\int_{x_{\mathrm{rec,m}}}^{x_{\mathrm{rec,M}}} f(x,t)dx \tag{13}$$

The value of $\overline{p}_0(t)$ is determined by calculating the time-averaged $\overline{p}(t)$ over a 2 ms window, which corresponds to approximately 10 periods of the experimentally measured instability. Regarding the other free parameters, x_c is set to 0 mm (as per Equation 6) and σ is assigned a value of 300 (as per Equation 10). The heat release calibration parameters, δ and T_r (as defined in Equation 6), are carefully selected to achieve the adiabatic flame temperature (T_{af}) under steady-state conditions (i.e., with the response function "switched off") at 15% of the chamber length. In the following, this specific parameters configuration is referred to as "Configuration A".

DOI: 10.13009/EUCASS2023-506

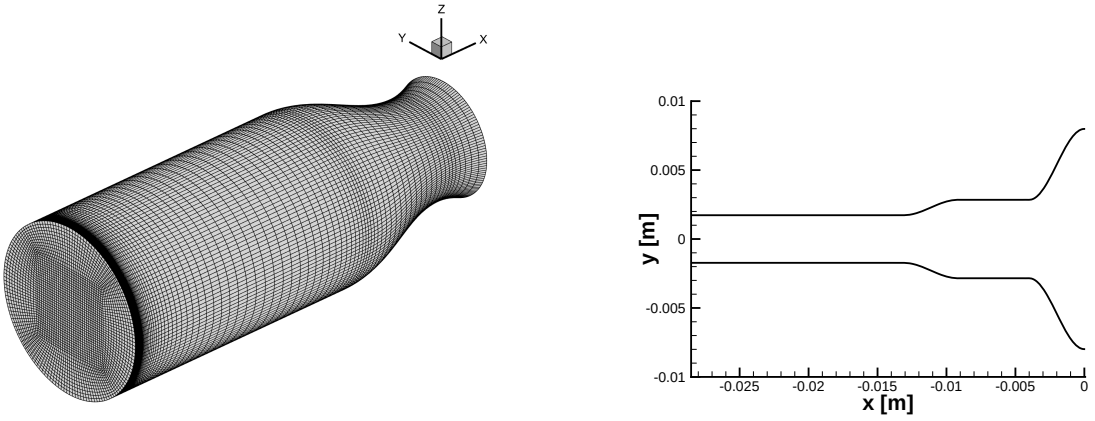

(a) NASA-LeRC 3D combustion chamber numerical grid.

(b) NASA-LeRC Q1D injector geometry.

Figure 5: Details of the NASA-LeRC domain in the hybrid-D framework.

The results obtained with Configuration A are presented in Figures 6 to 9. As shown in Figure 6, the hybrid-D model successfully captures the instability associated with the first tangential mode of the chamber. It is noteworthy to observe the spinning nature of this mode, characterized by a rotational displacement of the pressure nodal line with respect to the x-axis. Interestingly, this peculiar behavior aligns with experimental observations [5]. Another salient feature characterizing the computed instability is the coexistence of longitudinal dynamics alongside transverse dynamics. The pressure field, in its axial topology, exhibits a slight excitation of the first longitudinal chamber mode (1L). Consequently, the overall captured mode can be classified as a mixed 1T-1L mode. The lateral views of the pressure field, shown in Figure 7, provide invaluable insights into the intricate coupling dynamics between the combustion chamber and the injectors. When the azimuthal propagation of the high-pressure wave intersects an injector, a shock wave propagates upstream into the injector, resulting in the accumulation of fuel within the recessed region because of the action of the RF. Subsequently, the lack of fuel convected into the chamber determines strong off-stoichiometric conditions, resulting in an abrupt decrease in heat release rate. The gasdynamical consequence of this thermal event is the generation of an intense isotropic rarefaction. In particular, the rarefaction traveling upstream into the injector along the $u - a$ characteristic line determines the release of the accumulated fuel, closing the loop and starting a new thermoacoustic cycle. Hence, the model effectively captures the intricate thermoacoustic feedback mechanism.

The complex fuel accumulation and release process is illustrated in Figure 8, wherein the spatial distribution of temperature and fuel mass fraction within the chamber is depicted. The snapshots presented in Figure 8 correspond to the t_3 time instant reported in Figure 6. A complicated pattern emerges, showcasing alternating regions characterized by fuel-rich conditions (corresponding to fuel release) and oxidizer-rich regions (corresponding to fuel accumulation). These distinct zones are therefore characterized by mixture ratios deviating from stoichiometry. The reduced heat release associated with these mixture conditions results in lower temperature profiles within the chamber that can be observed in Figure 8a. It is interesting to emphasize that the independent response characteristics of each quasi-1D domain, owing to their distinct response functions, give rise to a pronounced phase difference among the convected fuel pockets. This azimuthal phase shift, that is an image of the spinning tangential nature of the examined instability, is at the base of the significant heterogeneity observed in the temperature and fuel mass fraction fields in Figure 8b.

Figure 9 reports the pressure signal sampled at the outer edge of the injection plate, together with its corresponding power spectral density (PSD). The typical temporal evolution of spontaneous thermoacoustic instability manifests prominently, characterized initially by an exponential growth of the oscillations' amplitude (Figure 9c), followed by the emergence of a limit cycle regime characterized by strong nonlinearities (Figure 9d). The pressure field exhibits a maximum peak-to-peak amplitude of 8.0 MPa, with an associated error of 60% when compared to experimental data. The dominant frequency of 5350 Hz is captured with an error margin of 2.5% relative to the experimental measurement. Therefore, while the model exhibits notable discrepancies in accurately capturing the amplitude of the observed instability, it achieves excellent agreement in terms of frequency with respect to the experimentally recorded values. It is worth noting that the amplitude discrepancy can be ascribed to the use of the ideal gas model. Indeed, as previously mentioned, in thermodynamic regimes characterized by supercritical pressure and subcritical temperature, the ideal gas model deviates significantly from more refined thermodynamic formulations, particularly in terms of acoustic impedance which can affect the amplitude of acoustic waves.

DOI: 10.13009/EUCASS2023-506

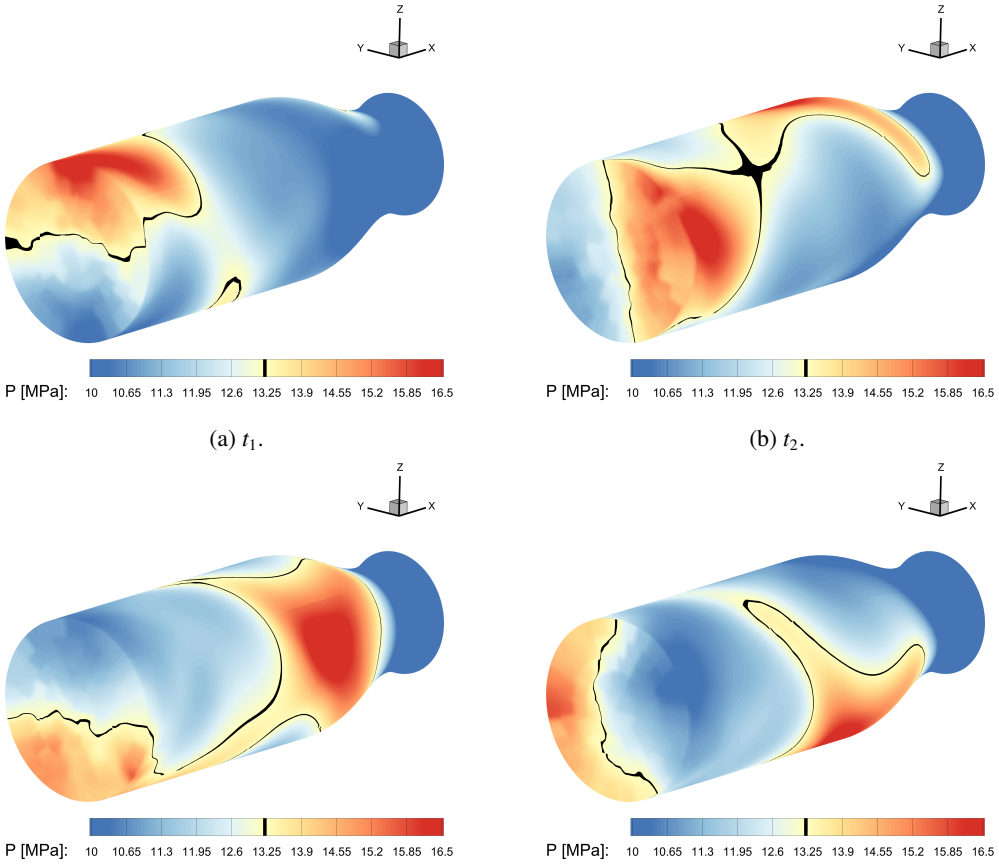

(a) t_1. (b) t_2.

(c) t_3. (d) t_4.

Figure 6: Chamber pressure field at 4 consecutive time instants.

In conclusion, the obtained results demonstrate the model capability to capture the essential characteristics of the thermoacoustic instability, including its temporal evolution and dominant frequency. While some discrepancies exist in accurately predicting the amplitude of the observed instability, the excellent agreement in terms of frequency with experimental measurements highlights the model potential for guiding the design and optimization of liquid rocket engines.

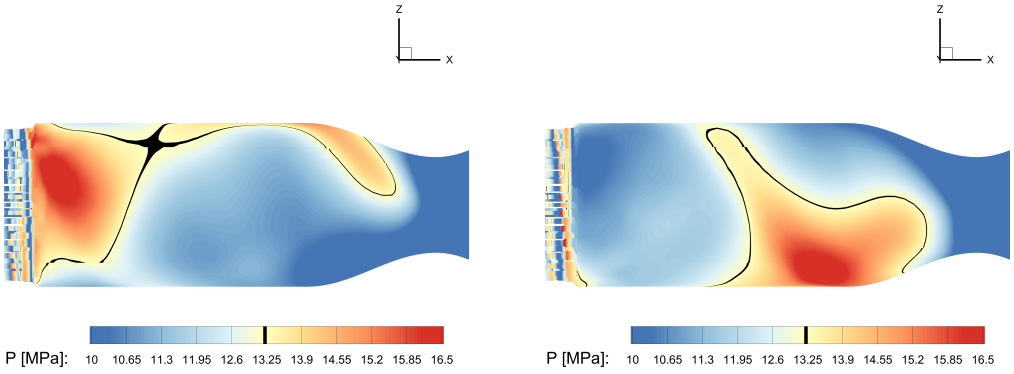

(a) t_2. (b) t_4.

Figure 7: Lateral view of pressure field at 2 time instants.

DOI: 10.13009/EUCASS2023-506

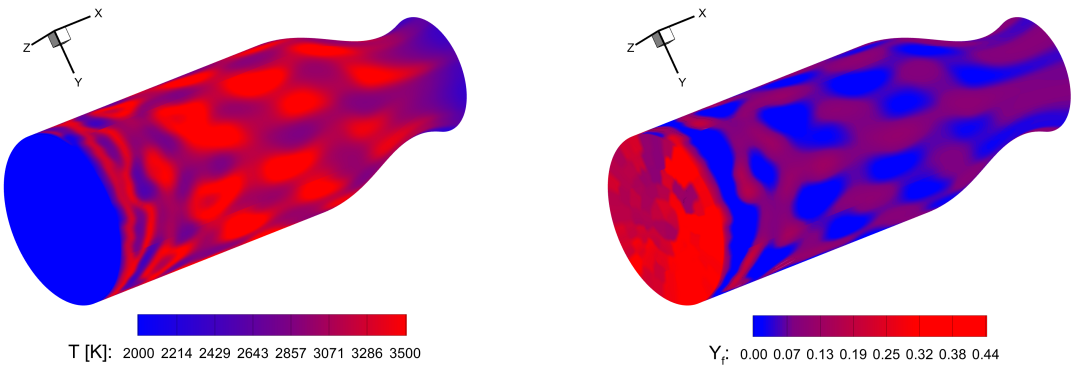

(a) Temperature.

(b) Fuel mass fraction.

Figure 8: Temperature and fuel mass fraction fields at t_3.

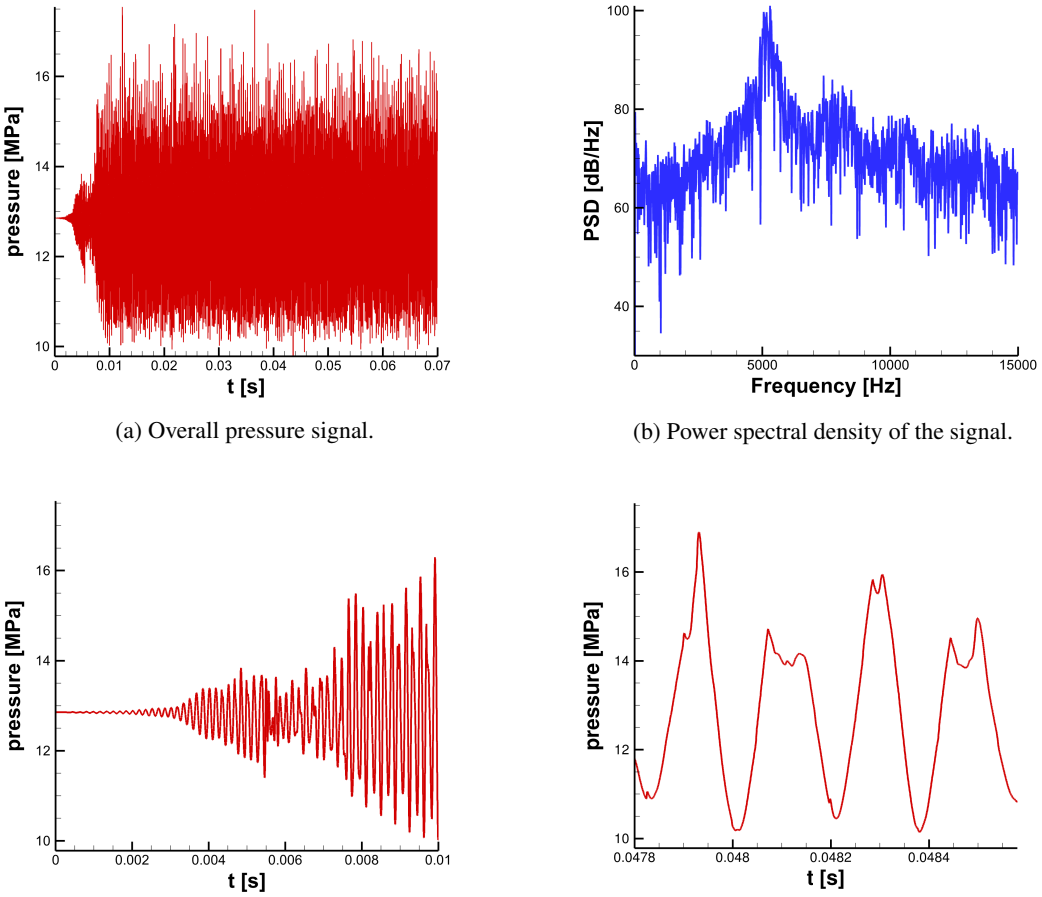

(a) Overall pressure signal.

(b) Power spectral density of the signal.

(c) Zoom on the initial exponential evolution.

(d) Zoom on the limit cycle.

Figure 9: Pressure signal sampled at the outer edge of the injection plate for Configuration A.

DOI: 10.13009/EUCASS2023-506

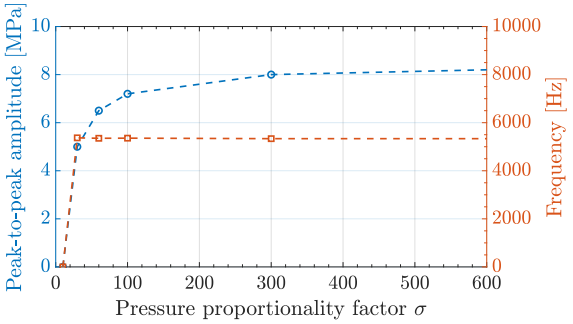

Figure 10: Limit cycle characteristics with respect to σ.

4.2 Parametric analyses

It is of paramount importance to conduct a thorough analysis of the sensitivity of the hybrid-D model to variations in the free parameters in order to properly understand its main dependencies. Specifically, the aim of the present work is to investigate the impact of the proportionality factor σ (Equation 10), the combustion starting abscissa x_c (Equation 6), the pressure sampling abscissa x_s (Equation 10), and the calibration parameters of the thermal release curve, namely δ and T_r (Equation 6). Throughout the subsequent analyses, the reference configuration against which these parameters are varied is the aforementioned Configuration A. All the pressure signals under consideration are sampled at the outer edge of the faceplate.

Regarding the dependence on the proportionality factor σ, Figure 10 portrays the obtained results in terms of the characteristics of the limit cycle. Both the peak-to-peak amplitude and the frequency exhibit a marked sensitivity to this parameter. Notably, exceedingly low values of σ yield a stable system. As σ increases, a plateau-like behavior emerges, signifying the insensitivity of the thermoacoustic characteristics to variations of the pressure proportionality factor beyond a particular threshold. This response function feature arises from its inherent structure (Equation 10): surpassing the case dependent threshold value of σ leads to a complete disruption of fuel flow during the accumulation phase, consequently determining the response function to reach a state of "saturation".

Figure 11 presents the results of the sensitivity analysis pertaining to the combustion starting abscissa x_c and the pressure sampling abscissa x_s, still in terms of peak-to-peak amplitude and frequency of limit cycle. The dependence of both the observables on x_c follows a similar trend: as x_c increases, the peak-to-peak amplitude and frequency decrease until system stability is attained for $x_c \geq 7.5$ mm (Figure 11a). The decrease in frequency is a direct consequence of the reduction in temperature near the faceplate, resulting in a diminished average speed of sound and, in turn, a decrease in the chamber acoustic eigenfrequencies. On the other hand, the amplitude drop for increasing x_c can be attributed not solely to the variation in the spatial-temporal lag between pressure oscillations and heat release, as per Rayleigh criterion [21], but also to potential numerical diffusion of slow fuel pockets owing to their larger distance traveled before combustion, together with the increase in axial cell size moving along the x-axis (Figure 5a). The pressure sampling abscissa x_s strongly affects thermoacoustic features. Indeed, it is shown in Figure 11b how limit cycles exhibit different behaviors for varying x_s, with notable fluctuations in peak-to-peak amplitude and frequency. This intricate phenomenology arises from the complicate interplay between the sampling location, the convective transport, and the heat release dynamics within the combustion chamber. The observed chaotic nature underscores the sensitivity of the thermoacoustic behavior to variations in the pressure signal sampling position and reinforces the decision to decouple the response function behavior from this parameter.

An analysis has also been conducted on the heat release curve calibration parameters, i.e. δ and T_r. A simulation has been performed by selecting these parameters in order to reach the adiabatic flame temperature at 5% of the combustion chamber. A comparison between the resulting pressure field and that obtained for Configuration A, where the adiabatic flame temperature is achieved at 15% of the combustion chamber, is shown in Figure 12. It can be observed that, although the amplitude of the pressure oscillations is comparable, the fields differ in their longitudinal dynamics. Indeed, it is recalled that the field obtained with Configuration A exhibits a 1L longitudinal dynamics superimposed on the dominant 1T mode, whereas in the current case the longitudinal activity is of 2L type. This difference translates spectrally into an increase in the dominant frequency, which is equal to 6182 Hz for the new setup (see Figure 13).

Given the significance demonstrated by the spatial/temporal lag between x_c and x_s, the engine stability behavior

DOI: 10.13009/EUCASS2023-506

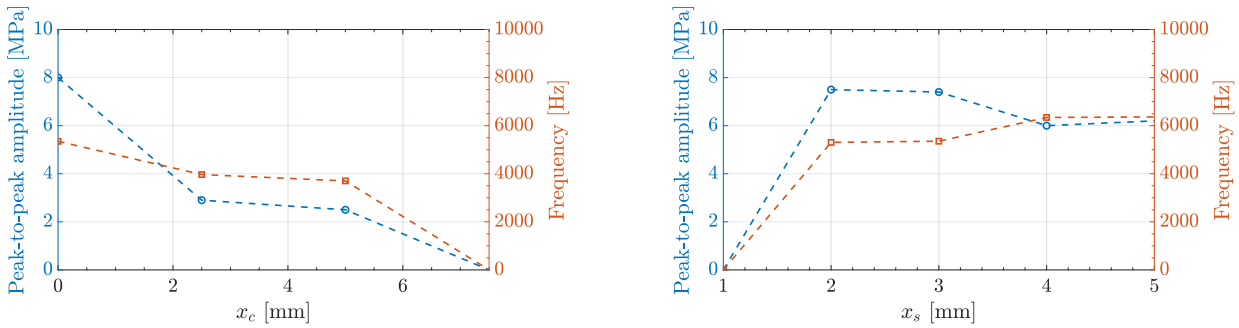

(a) Peak-to-peak amplitude and frequency dependency on x_c.

(b) Peak-to-peak amplitude and frequency dependency on x_s.

Figure 11: Limit cycle characteristics as functions of x_c and x_s.

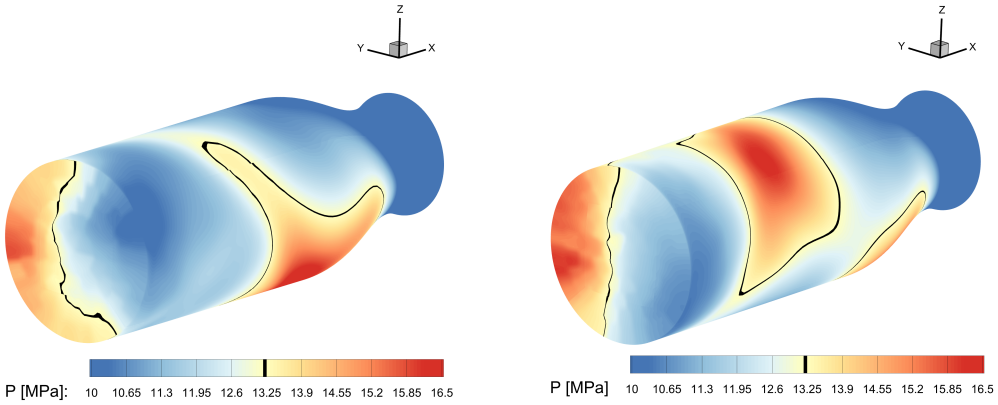

(a) T_{af} at 15% of the chamber length.

(b) T_{af} at 5% of the chamber length.

Figure 12: Chamber pressure field for different heat release curves.

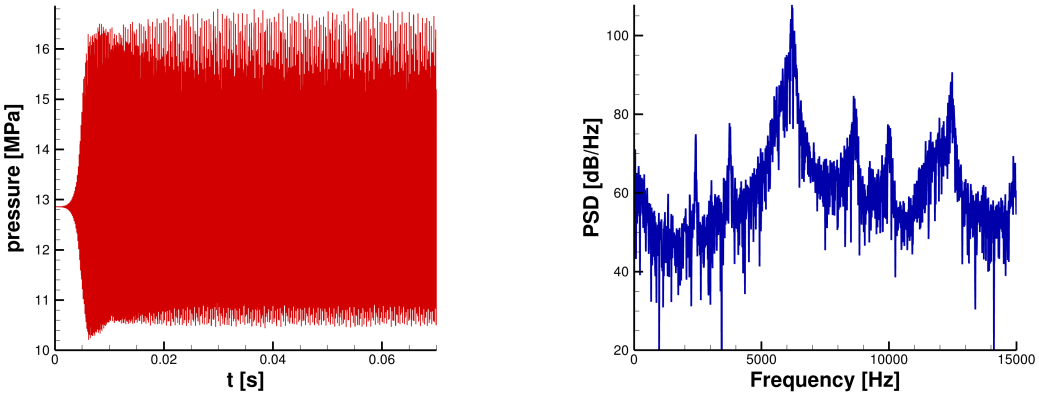

(a) Overall pressure signal.

(b) Power spectral density of the signal.

Figure 13: Pressure signal sampled at the outer edge of the injection plate, T_{af} at 5% of the chamber length.

DOI: 10.13009/EUCASS2023-506

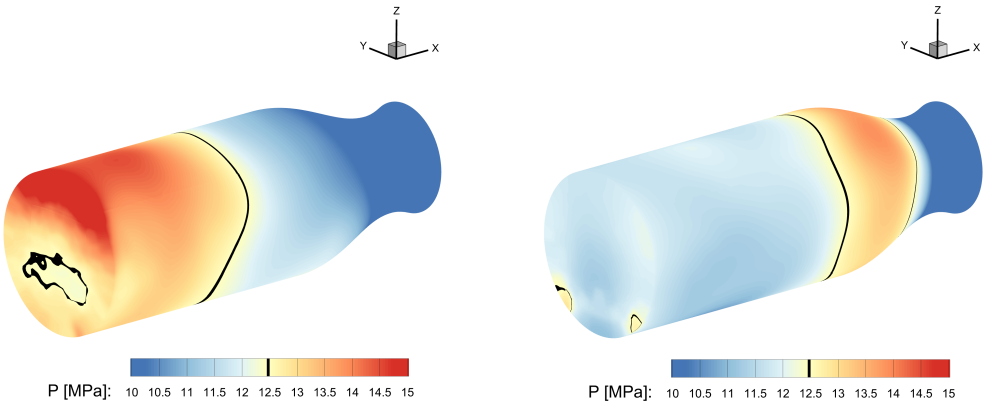

(a) t_1. (b) t_2.

Figure 14: Chamber pressure field at 2 consecutive time instants, doubled recess.

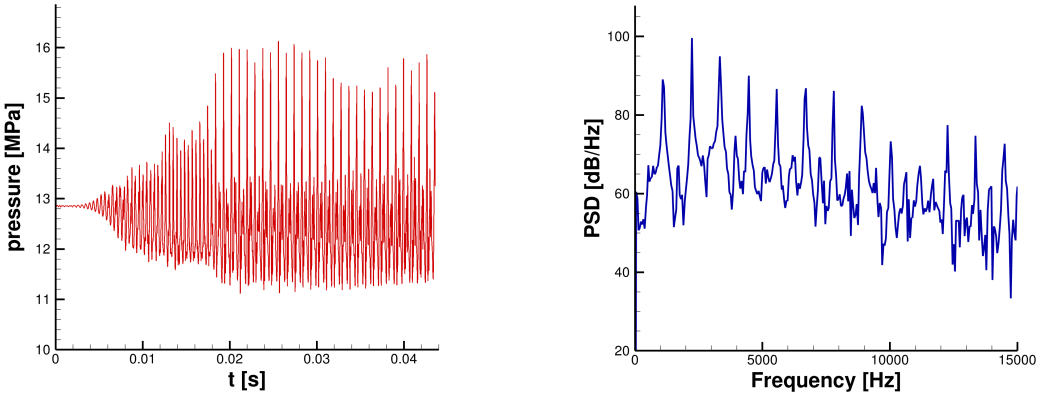

(a) Overall pressure signal. (b) Power spectral density of the signal.

Figure 15: Pressure signal sampled at the outer edge of the injection plate, doubled recess.

has been investigated in a modified geometrical configuration. Specifically, the length of the recess has been doubled while maintaining the overall length of the injectors. The thermo-fluid dynamic consequence of this geometrical change is twofold: on the one hand, the distance traveled by each fuel pocket before combustion is doubled and, on the other hand, the evolution of flow variables inside the recess is quantitatively different, resulting in a slight change of the injector longitudinal frequency. Both the effects imply a variation in the spatial/temporal lag between pressure and heat release oscillations, at the core of the thermoacoustic instability self-sustaining nature. As shown in Figure 14, the new configuration is still unstable but exhibits pronounced variations in the characteristics of the associated limit cycle. In particular, the instability primarily affects the first longitudinal mode of the combustion chamber (1L), with a dominant frequency of 2240 Hz and a peak-to-peak amplitude of the pressure signal equal to 50 bar, as shown in Figure 15. This result further emphasizes the key roles played by the injector design and the pressure/heat release oscillations lag in determining the onset and the thermoacoustic characteristics of the instability.

In conclusion, the conducted sensitivity analysis offers valuable insights into the complex relationships between the different free parameters and the thermoacoustic behavior of the 1D-3D model. These findings play a vital role in refining the model and improving its predictive capabilities for practical applications.

4.3 Baffles

Having thoroughly investigated the behavior of the hybrid-D model in a geometrically complex configuration, it is crucial, for the purpose of assessing the predictive capability of the methodology, to examine its ability to discern between stable and unstable setups. Thus, the capacity to distinguish stability from instability is examined by introducing damping devices within the combustion chamber. In the framework of LREs, baffles and acoustic cavities have been

DOI: 10.13009/EUCASS2023-506

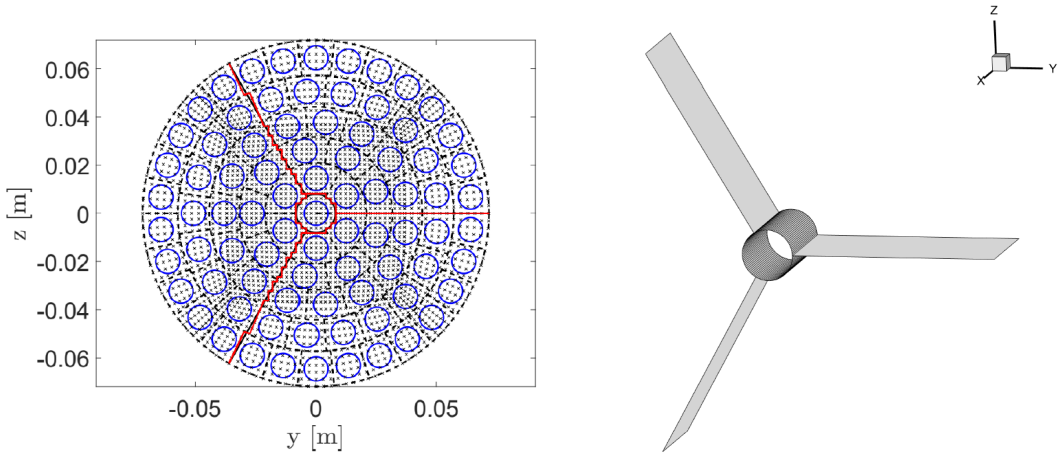

(a) Baffles projection on the faceplate.

(b) Three dimensional view of the baffles.

Figure 16: Details on the disposition and geometry of the baffles used for the NASA-LeRC engine.

widely employed as common means of controlling and damping HF combustion instability [16, 1]. Specifically, due to their historical usage and effectiveness in stabilizing tangential modes [2], baffles are implemented and analyzed within the hybrid-D formulation.

From a modeling standpoint, baffles are treated as infinitesimally thin solid walls immersed within the flow field. Once the number and arrangement of baffles within the chamber are determined, they are embedded as wall boundary conditions on the transverse plane relative to the x-axis. Figure 16 depicts the geometric characteristics of the 3-baffle configuration adopted as a test case in the present work. Following the guidelines reported in [22], the baffle length is set equal to 20% of the chamber diameter. The free parameters characterizing the low-order model are held constant, adhering to the specifications outlined in Configuration A.

The obtained results in terms of chamber pressure field are shown in Figure 17, clearly evidencing the presence of the three baffles and their consequential impact on the pressure field topology. In particular, the pressure field undergoes notable distortion compared to the characteristic symmetry of the first tangential chamber mode. The azimuthal high-pressure wave associated with the instability interacts with the baffles, resulting in partial reflection and partial bypassing of such solid obstacles. The influence of this gasdynamically rich phenomenology on the thermoacoustic characteristics of the engine is presented in Figure 18, which showcases the pressure signal acquired at the outer edge of the injection plate. A comparison of this signal with that shown in Figure 6 reveals a reduction in the peak-to-peak amplitude by 20 bar (from 80 bar to 60 bar). Furthermore, the altered structure of the pressure field leads to a variation in the dominant frequency, which amounts to 5800 Hz in the case with baffles, in contrast to the 5350 Hz observed in the configuration without baffles. The increase in the limit cycle frequency and decrease in amplitude aligns well with the partial decrease in the available space for the propagation of pressure waves, as they are partially reflected due to the interaction with solid walls. This interaction hinders the spinning mode of the waves, resulting in a reduction of the associated energy and amplitude.

In conclusion, despite the use of these dampers did not result in the stabilization of the engine, a marked reduction in the intensity of pressure oscillations is observed, as well as a variation in the dominant frequency resulting from the symmetry breakage. It is worth emphasizing that a comprehensive assessment of engine stabilization through baffles would need an extensive parametric analysis encompassing the number, geometry, and arrangement of the baffles within the chamber, which is out of the scope of the present preliminary analysis. Moreover, a thorough assessment of the solver behavior with baffles would require access to a substantial amount of experimental data especially on the reference test case, which is currently unavailable.

5. Conclusions

In this study, a comprehensive analysis of the thermoacoustic behavior in a 1D-3D model of a reference combustor is presented. The model successfully captures the complex interplay between acoustic and combustion dynamics, providing valuable insights into the underlying phenomena. The sensitivity analysis conducted on the RF free parameters and on the geometry of the system has revealed their significant impact on the thermoacoustic behavior. The choice of the injector design, the proportionality factor σ, the heat release curve calibration parameters δ and T_r, the com-

DOI: 10.13009/EUCASS2023-506

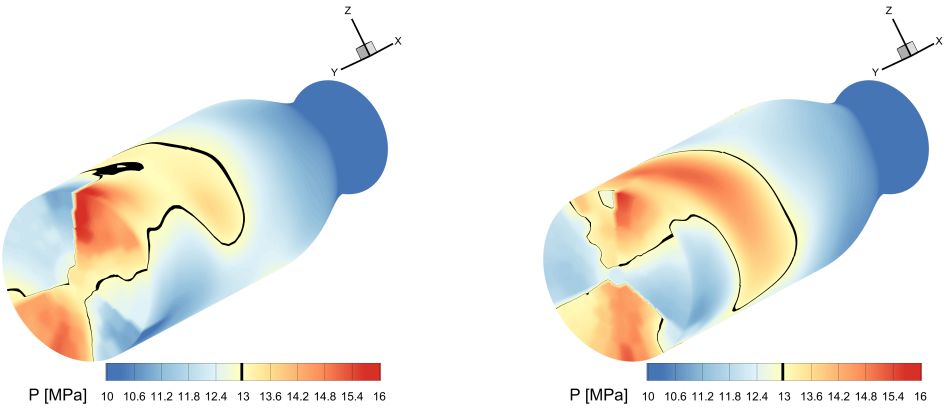

(a) t_1. (b) t_2.

Figure 17: Chamber pressure field at 2 consecutive time instants using baffles.

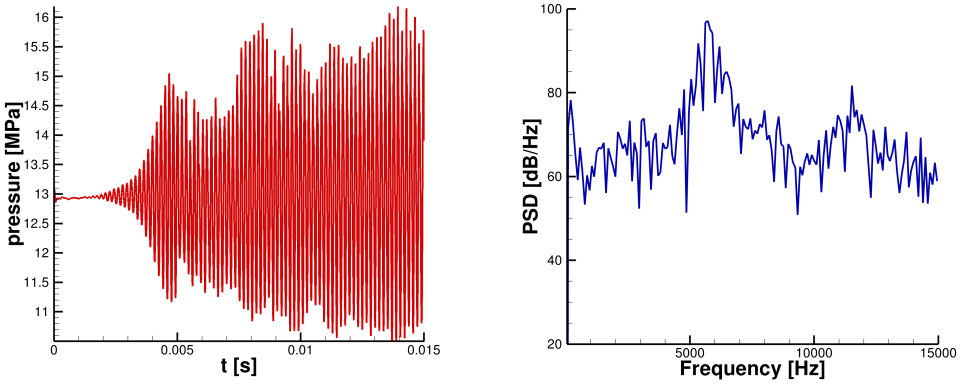

(a) Overall pressure signal. (b) Power spectral density of the signal.

Figure 18: Pressure signal sampled at the outer edge of the injection plate using baffles.

bustion starting location x_c, and the sampling point x_s, proved to be crucial in capturing the desired acoustic features. The results emphasize the need for careful parameter selection to accurately represent the unstable dynamics in the ideal gas framework. The investigation on baffles has demonstrated their consequential impact on the pressure field topology. Their presence alters the symmetry of the pressure field, resulting in a reduction in peak-to-peak amplitude and a variation in the dominant frequency. This result underscores the capability of the model to identify the presence and impact of damping devices. Future work should focus on expanding the parameter space exploration, considering additional design factors, such as the geometry and arrangement of baffles, as well as incorporating more refined thermodynamic formulations to capture the behavior in regimes characterized by supercritical pressure and subcritical temperature. Furthermore, experimental validation and comparison with a wider range of data are essential to further enhance the predictive capabilities of the model. In conclusion, this study contributes to the understanding of thermoacoustic instabilities in combustion systems and provides valuable insights for the development of effective control and design strategies in practical applications.

6. Acknowledgments

This research was jointly funded by Sapienza University and the Italian Space Agency - Agenzia Spaziale Italiana (ASI) as part of the research N.2019-4-HH.0, project no. (CUP) F86C17000080005, carried out under the framework agreement N.2015-1-Q.0.

References

[1] S. D. Heister, W. E. Anderson, T. L. Pourpoint, and R. J. Cassady, *Rocket propulsion*, vol. 47. Cambridge University Press, 2019.

DOI: 10.13009/EUCASS2023-506

[2] F. E. Culick and V. Yang, "Overview of combustion instabilities in liquid-propellant rocket engines," 1995.

[3] S. Gröning, J. S. Hardi, D. Suslov, and M. Oschwald, "Injector-driven combustion instabilities in a hydrogen/oxygen rocket combustor," *Journal of Propulsion and Power*, vol. 32, no. 3, pp. 560–573, 2016.

[4] Y. C. Yu, J. C. Sisco, S. Rosen, A. Madhav, and W. E. Anderson, "Spontaneous longitudinal combustion instability in a continuously-variable resonance combustor," *Journal of Propulsion and Power*, vol. 28, no. 5, pp. 876–887, 2012.

[5] R. Jensen, H. Dodson, and S. Claflin, "Lox/hydrocarbon combustion instability investigation," tech. rep., National Aeronautics and Space Administration, 1989.

[6] A. Urbano, L. Selle, G. Staffelbach, B. Cuenot, T. Schmitt, S. Ducruix, and S. Candel, "Exploration of combustion instability triggering using large eddy simulation of a multiple injector liquid rocket engine," *Combustion and Flame*, vol. 169, pp. 129–140, 2016.

[7] M. E. Harvazinski, C. Huang, V. Sankaran, T. W. Feldman, W. E. Anderson, C. L. Merkle, and D. G. Talley, "Coupling between hydrodynamics, acoustics, and heat release in a self-excited unstable combustor," *Physics of Fluids*, vol. 27, no. 4, p. 045102, 2015.

[8] S. Srinivasan, R. Ranjan, and S. Menon, "Flame dynamics during combustion instability in a high-pressure, shear-coaxial injector combustor," *Flow, Turbulence and Combustion*, vol. 94, pp. 237–262, 2015.

[9] L. Crocco and S.-I. Cheng, "Theory of combustion instability in liquid propellant rocket motors," tech. rep., Princeton Univ Nj, 1956.

[10] Y. Yu, J. Sisco, V. Sankaran, and W. Anderson, "Effects of mean flow, entropy waves, and boundary conditions on longitudinal combustion instability," *Combustion Science and Technology*, vol. 182, no. 7, pp. 739–776, 2010.

[11] M. L. Frezzotti, F. Nasuti, C. Huang, C. L. Merkle, and W. E. Anderson, "Quasi-1d modeling of heat release for the study of longitudinal combustion instability," *Aerospace Science and Technology*, vol. 75, pp. 261–270, 2018.

[12] S. D'Alessandro, M. L. Frezzotti, B. Favini, and F. Nasuti, "Driving mechanisms in low-order modeling of longitudinal combustion instability," *Journal of Propulsion and Power*, pp. 1–11, 2023.

[13] P. M. Zolla, A. Montanari, S. D'Alessandro, M. Pizzarelli, and F. Nasuti, "Low order modeling of combustion instability using a hybrid real/ideal gas mixture model," in *9th EUCASS*, 2022.

[14] S. D'Alessandro, G. Fedeli, F. Tonti, J. Hardi, M. Oschwald, B. Favini, and F. Nasuti, "Low-order modeling of combustion instability applied to cryogenic propellants," in *8th EUCASS*, 2019.

[15] S. D'Alessandro, M. L. Frezzotti, B. Favini, and F. Nasuti, "A multi-dimensional approach for low order modeling of combustion instability in a rocket combustor," in *2018 Joint Propulsion Conference*, p. 4677, 2018.

[16] W. Armbruster, J. S. Hardi, Y. Miene, D. Suslov, and M. Oschwald, "Damping device to reduce the risk of injection-coupled combustion instabilities in liquid propellant rocket engines," *Acta Astronautica*, vol. 169, pp. 170–179, 2020.

[17] M. L. Frezzotti, F. Nasuti, C. Huang, and W. E. Anderson, "Extraction of response function from numerical simulations and their use for longitudinal combustion intsbility modeling," in *55th AIAA Aerospace Sciences Meeting*, p. 1338, 2017.

[18] B. McBride and S. Gordon, "Computer program for calculation of complex chemical equilibrium compositions and applications," *NASA RP–1311, October*, 1994.

[19] P. Glaister, "An approximate linearised Riemann solver for the three-dimensional Euler equations for real gases using operator splitting," *Journal of computational physics*, vol. 77, no. 2, pp. 361–383, 1988.

[20] S.-K. Kim, H.-S. Choi, and Y. Kim, "Thermodynamic modeling based on a generalized cubic equation of state for kerosene/lox rocket combustion," *Combustion and flame*, vol. 159, no. 3, pp. 1351–1365, 2012.

[21] J. W. S. B. Rayleigh, "The explanation of certain acoustical phenomena," *Nature*, vol. 18, no. 455, pp. 319–321, 1878.

[22] J. Muss, T. Nguyen, and C. Johnson, "User's manual for rocket combustor interactive design (ROCCID) and analysis computer program. volume 1: User's manual," tech. rep., National Aeronautics and Space Administration, 1991.